Supporting Information

Tuning the Lattice Parameter of In_xZn_yP for Highly Luminescent Lattice-Matched Core/Shell Quantum Dots

Francesca Pietra[a*], *Luca De Trizio*[c], *Anne W. Hoekstra*[a], *Nicolas Renaud*[a], *Mirko Prato*[c], *Ferdinand C. Grozema*[a], *Patrick J. Baesjou*[d], *Rolf Koole*[d], *Liberato Manna*[b,c] *and Arjan J. Houtepen*[a].

[a]Opto-Electronic Materials Section, Faculty of Applied Sciences, Delft University of Technology, Julianalaan 136,2628 BL Delft, The Netherlands

[b]Kavli Institute of Nanoscience, Delft University of Technology Lorentzweg 1 2628 CJ Delft, The Netherlands

[c]Department of Nanochemistry, Istituto Italiano di Tecnologia (IIT), via Morego, 30, 16163 Genova, Italy

[d]Philips Research Laboratories, High Tech Campus 4, 5656 AE Eindhoven, The Netherlands

[e]Soft Condensed Matter, Debye Institute, Utrecht University, Princetonplein 5, 3584 CC Utrecht, The Netherlands

* Corresponding author

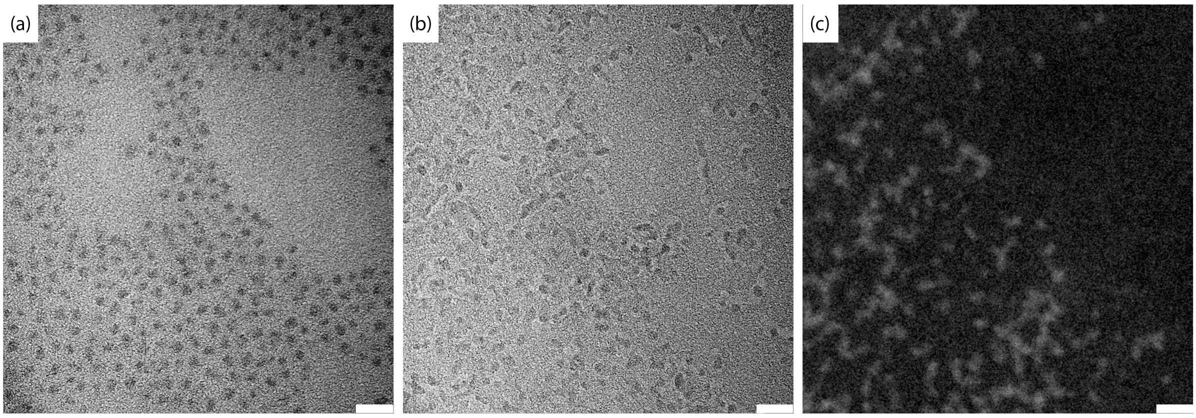

Figure S1- TEM images and STEM of In_xZn_yP QDs with (a) Zn/In:0, d:2.7±0.3 nm and (b) Zn/In:1, d:2.9±0.2 nm. (c) Zn/In:4, d:2.6±0.3 nm. Scale bar 10nm. The sized difference between the three samples is within the standard deviation, therefore we can conclude that the NCs'size does not change by varying the concentrations of Zn.

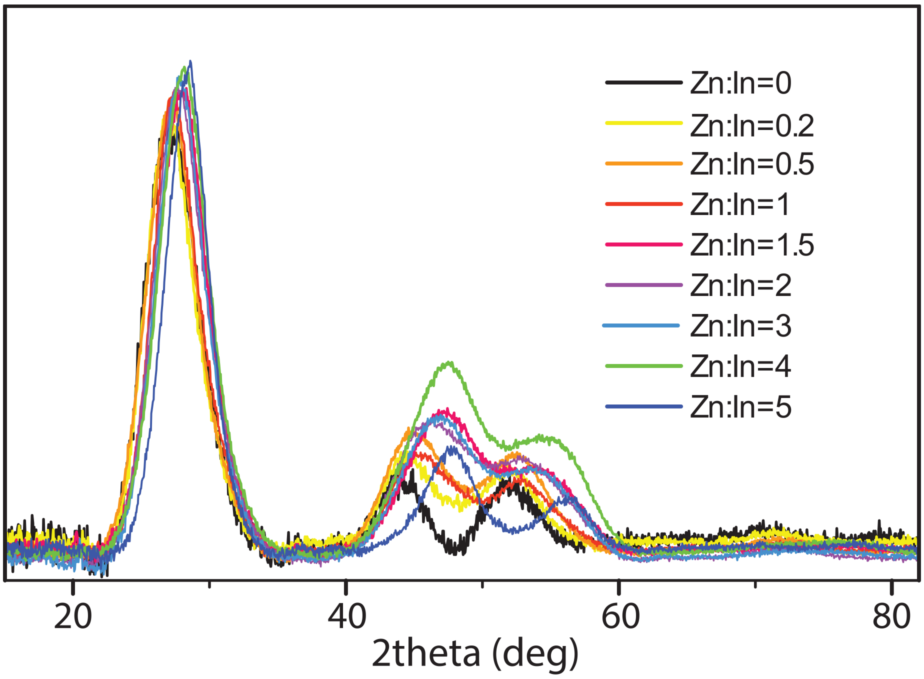

Figure S2- XRD patterns obtained from drop-cast solutions of In_xZn_yP NCs, with different initial Zn feed ratios, from Zn/In:0 to Zn/In:5.

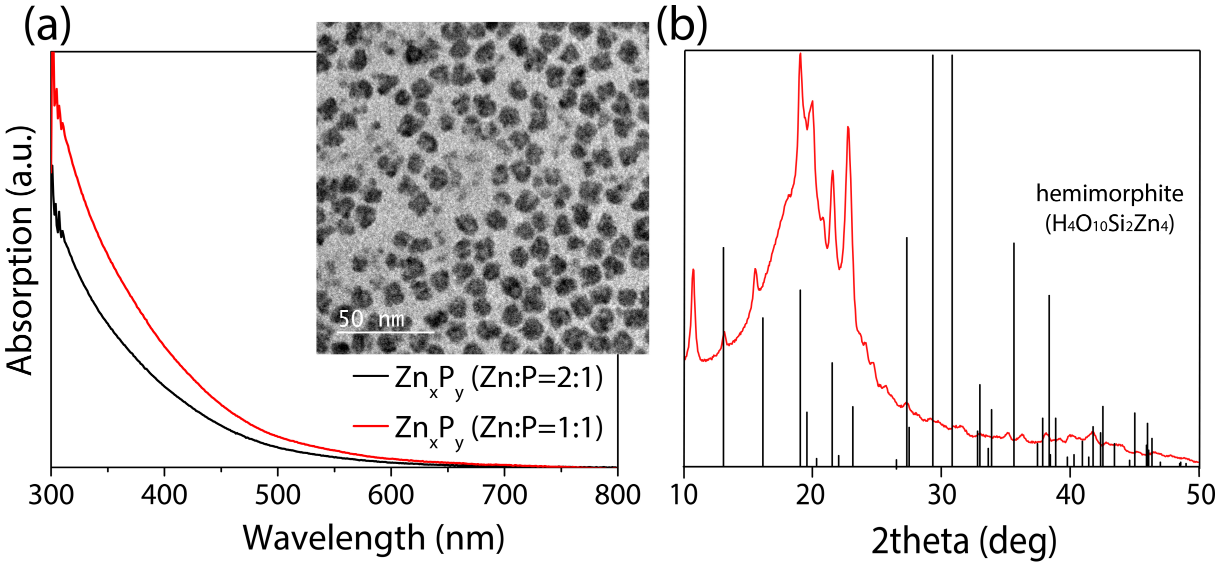

Figure S3 (a) Absorption spectra of synthesised Zn_xP_y NCs with different Zn/P ratios. Inset: TEM image of a Zn_xP_y sample. (b) corresponding XRD pattern of the Zn_xP_y NCs, along with the bulk pattern of hemimorphite.

Theoretical calculations

The XRD spectrum obtained with different basis set and XC functionals for a 1.50 nm InP quantum dots are represented in Fig. S-9. As seen in this figure, the positions of the peaks are not significantly affected by changes of the basis set size or functional types. We have kept in our calculation a small double-zeta (DZ) basis set with large frozen cores and the local density approximation (LDA) XC-functional. We have performed geometry optimization at the DFT (DZ/LDA) level of theory for 4 different sizes of InP quantum dots. The corresponding geometries and XRD spectra are represented in Fig. S10. As seen in this figure, the positions of the XRD peaks roughly correspond to the ones observed experimentally. As expected these peaks become increasingly marked as the size of the NC increases.

We have then progressively introduced Zn atoms in the composition of the NCs following the two approaches outlined above. Representative XRD spectra obtained following these methods are shown in Fig. 11. Using the first approach, where only substitutional Zn atoms are used, we obtained a significant shift of the XRD peaks toward the higher angles. The magnitude of this shift is comparable with those obtained experimentally. In contrast, when using the second approach where both substitutional and interstitial Zn atoms are used, we obtained a smaller shift of the XRD peaks (in particular the first XRD peak) that is inconsistent with our experimental results. Note that in all cases the XRD peaks broaden due to the disorder induced by the introduction of Zn.

A coordination analysis was finally performed to characterize the modification of the bond lengths induced by the introduction of substitutional and interstitial zinc atoms. Graphical representations of this analysis are shown in Fig. 12-14. Fig. 12 shows the impact that substitutional Zn atoms have on the bond length of a small NCs. As seen in this figure the Zn-P bond length is up to 10 % smaller than the average In-P bond length of 2.65 A. Additionally, it appears that the introduction of Zn affects In-P bonds located in the vicinity of the additional zinc atoms due to the local distortion of the electronic density. Consequently, the introduction of Zn atoms not only affects the lattice at the substituted sites but also modifies the lattice parameters across the entire NC.

The impact of interstitial zinc introduction in a small quantum dots is illustrated in Fig. 13. Due to the small size of this NC the crystal structure is able to significantly rearrange to accommodate for the presence of interstitial Zn atoms. This rearrangement leads to a broad distribution of bond length across the NC, some shorter and some longer than the average In-P bond. For example, the middle panel shows that the interstitial zinc atom has significantly displaced a neighbouring indium atom, leading to a strong local distortion of the crystal structure.

The impact of interstitial zinc is more straightforward to analyse in larger NCs as represented in Fig. 14. There, the additional zinc atom simply leads to a local expansion of the In-P bonds in its direct vicinity. In all cases represented in Fig. 13 and 14 the introduction of interstitial zincs attenuate the reduction of the lattice parameter induced by the presence of substitutional zinc atoms. This explains the smaller shift observed in the XRD spectra of these NCs compared to those obtained considering substiutional zinc atoms only.

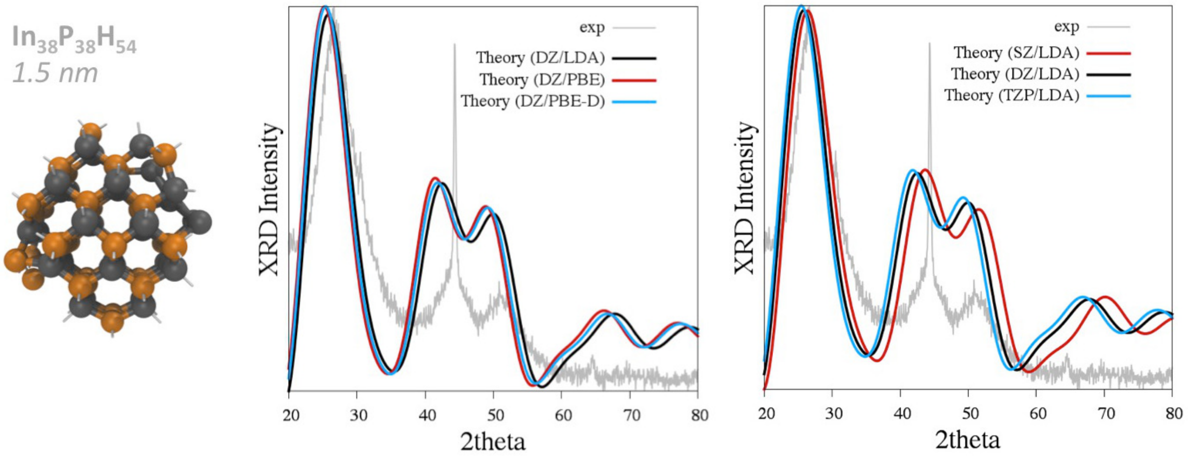

Figure S4 – Simulated XRD spectra obtained using different basis set and functionals for the geometry optimized InP quantum dots represented on the left. In, P and H atoms are represented in grey, orange and white respectively.

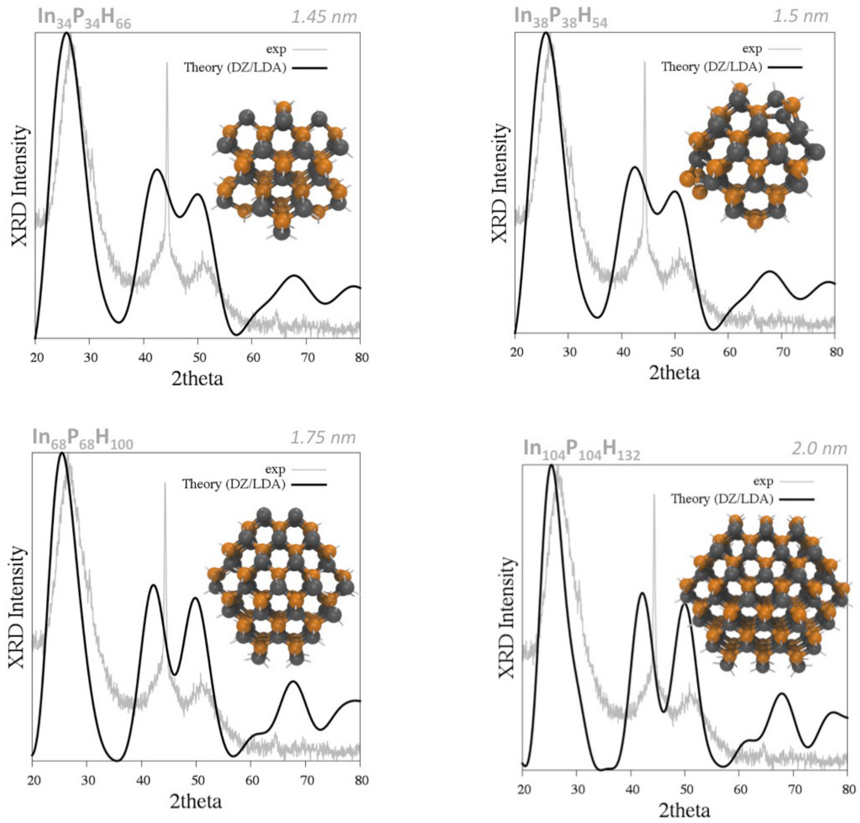

Figure S5– Simulated XRD Spectra for the 4 different sizes of InP NCs studied here. Each NC is represented in insert. In, P and H atoms are represented in grey, orange and white respectively.

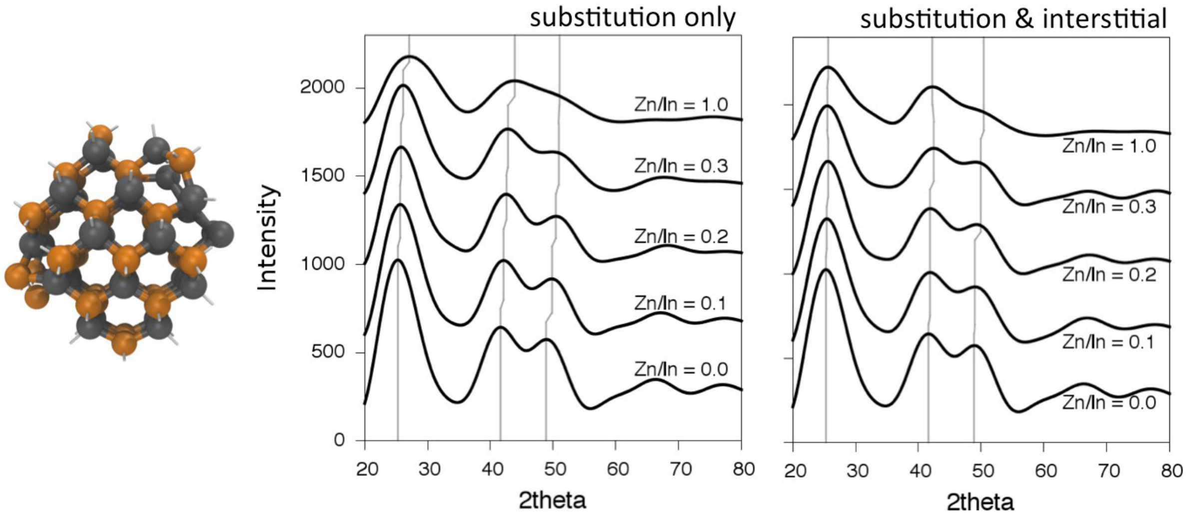

Figure S6 – Comparison of the simulated XRD spectra obtained upon introduction of only substitutional or both substitutional and interstitial Zn atoms in the composition of a 1.5 nm InP NC.

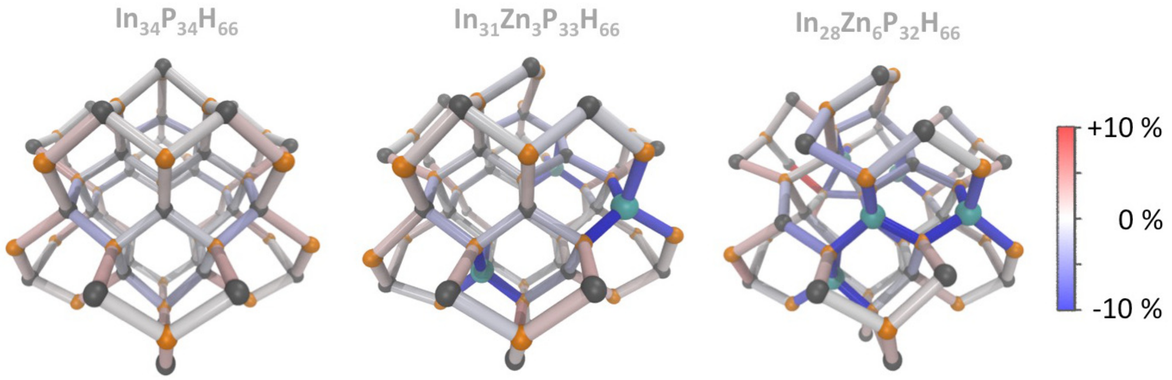

Figure S7 – Modification of the bond length within a 1.45 nm diameter QD upon introduction of substitutional Zinc atoms. The colour of the bonds represents the deviation of their length from the average In-P bond length (2.65 Ang.). In, Zn and P atoms are represented in grey, orange and cyan respectively. The hydrogen atoms are not shown for clarity.

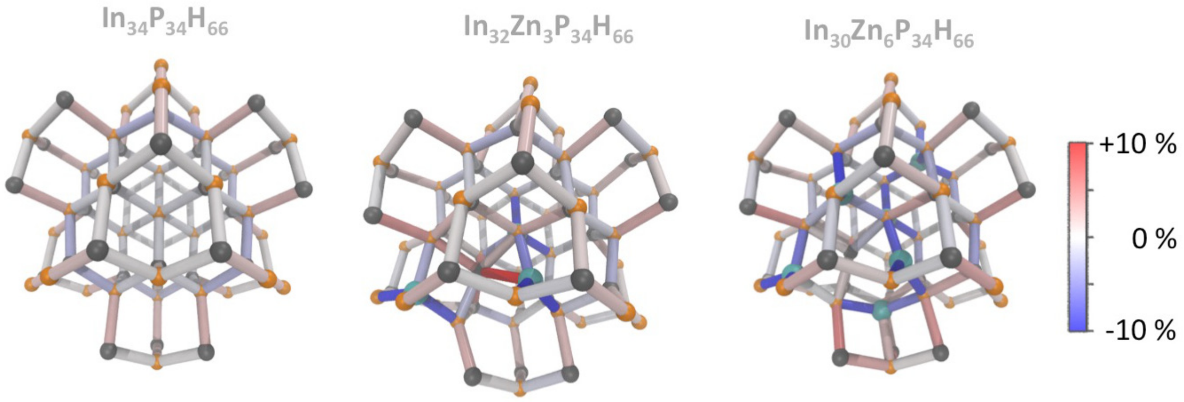

Figure S8 – Modification of the bond length within a 1.45 nm diameter QD upon introduction of substitional and interstitial Zinc atoms. The colour of the bonds represents the deviation of their length from the average In-P bond length (2.65 Ang.). In, Zn and P atoms are represented in grey, orange and cyan respectively. The hydrogen atoms are not shown for clarity.

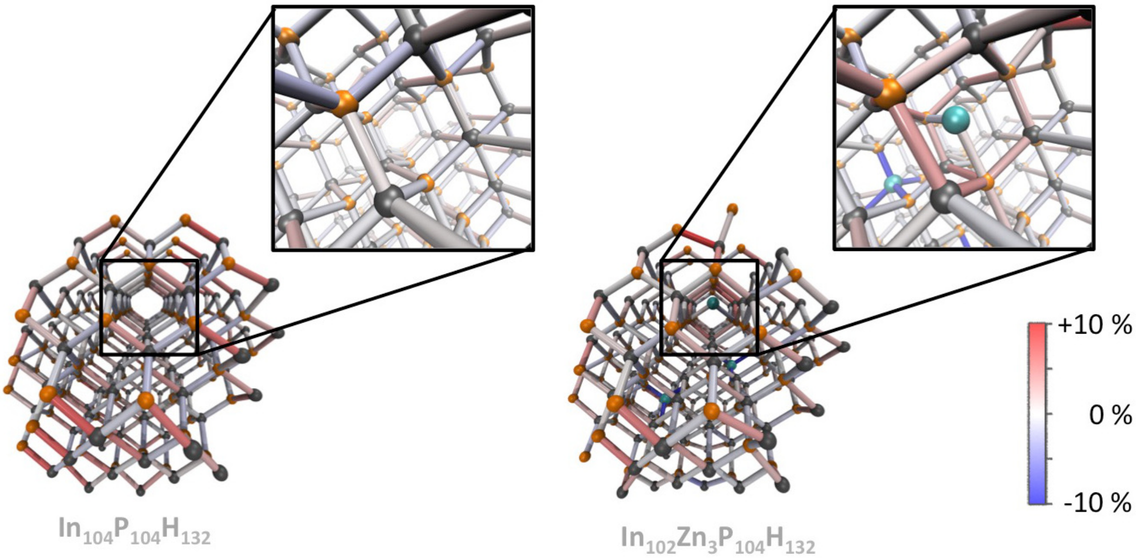

Figure S9 – Modification of the bond length within a 2.00 nm diameter QD upon introduction of 2 substitutional and 1 interstitial Zinc atoms. The colour of the bonds represents the deviation of the In-P bond length from the average value of 2.65 Å. In, Zn and P atoms are represented in grey, orange and cyan respectively. The hydrogen atoms are not shown for clarity.

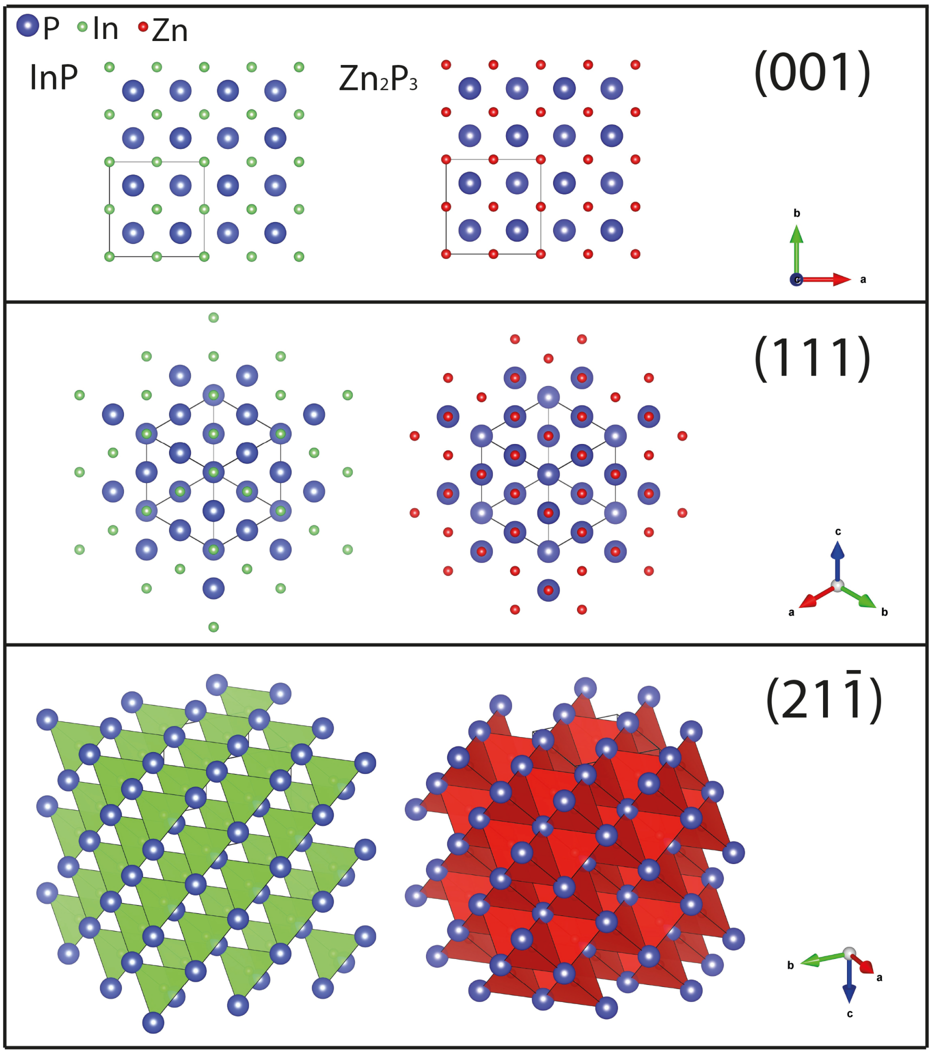

Figure S10 - Atomic sketches representing the zinc blende InP (left side) and cubic Zn_3P_2 (right side) crystal structures projected along the [001] (upper panel), [111] (middle panel) and [21-1] (lower panel) directions. Both materials are characterized by an FCC anionic P sublattice in which the only difference stands in the P-P bond length, which is shorter (4.016 Å) in the case of Zn_3P_2, compared to the case of InP (4.152 Å). In both materials the cations adopt a tetrahedral configuration. As the InP structure has to accommodate fewer cations, only the T+ tetrahedral sites are occupied, while in the case of Zn_3P_2 also a part of the T- sites are occupied, as evident in the lower panel. The structural isomorphism of the two phases is evident. The projection of the primitive unit cell is depicted with a solid black line in both structures.

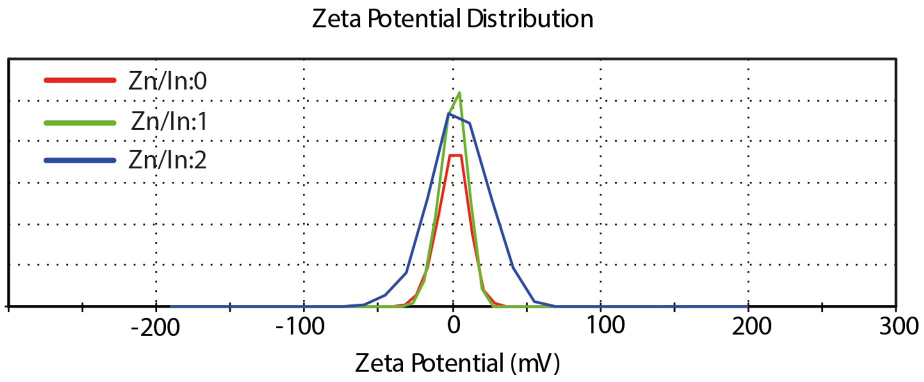

Figure S11- ζ-potential distribution for In_xZn_yP NCs prepared at different Zn/In feed ratios (Zn/In:0, red curve; Zn/In:1, green curve; and Zn/In:2, blue curve).

Table S1- TEM-EDX results on In_xZn_yP QDs.

Zn/In	In (%)	P(%)	Zn(%)
0	73	27	-
0.3	57	25	17
1.3	35	19	45

Table S2- Full width half maximum values (FWHM) for the PL emission peaks for In_xZn_yP cores with different concentrations of Zn. We take the standard deviation from 3 measurements.

Zn/In feed ratio	FWHM (nm)
0	79 ± 5
0.2	80 ± 7
0.5	69 ± 8
1	72 ± 4
1.5	69 ± 8
2	70 ± 10
3	79 ± 5
4	68 ± 7

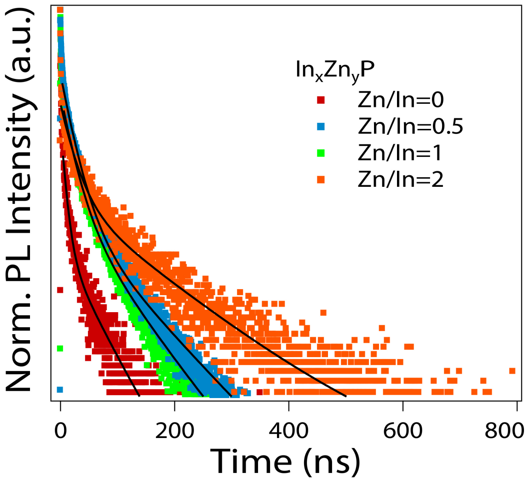

Figure S12-PL decay curve of In_xZn_yP NCs with different Zn^{2+} precursor concentrations, while monitoring the higher energy PL. Fitting a biexponential to the data (black curve) yields a fast component (τ_1) and a slow component (τ_2). The values of τ_1 and τ_2 for each samples are displayed in table 2 with the relative amplitude.

Table S3- Values of τ_1 and τ_2 for each In_xPZn_{x-1} samples (ns) with the relative amplitude (%).

Zn/In	**τ_1**	**A_1**	**τ_2**	**A_2**
0	8.1	0.23	65	0.05
0.5	15	0.32	96	0.16
1	11	0.29	81	0.19
2	18	0.21	129	0.16

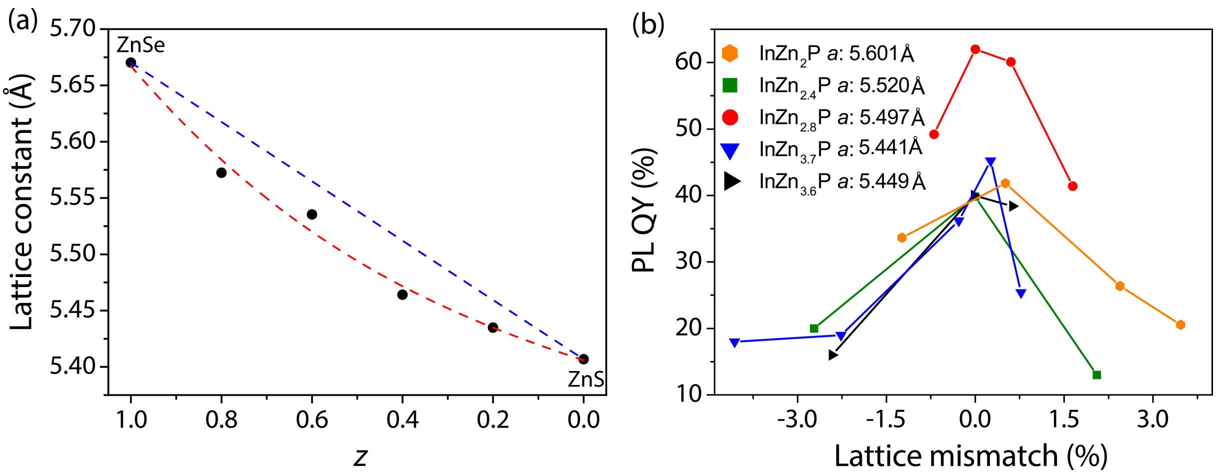

Figure S13-(a) Plot of the lattice constant of the $ZnSe_zS_{1-z}$ shell as function of the composition z.[1] (b) Plot of the PL QY as function of the lattice mismatch between In_xZn_yP cores with different concentration of Zn and the $ZnSe_zS_{1-z}$ shell. For each core, the highest PL QY value is reached when the lattice mismatch is 0%.

Figure S13a plots the lattice constant of the $ZnSe_zS_{1-z}$ shell as a function of the composition z as reported in reference 1. Ideally, z varies from ZnSe to ZnS linearly *via* Vegard's law[2] (blue dashed line), but the trend can deviate from linearity by a bowing parameter (b),[3,4] according to equation (1).

$$y = (1 - z) * 5.406 + z * 5.670 - b * x * (1 - x) \qquad \text{eq. 1}$$

where 5.406 is the lattice constant of ZnS (Å) [1] and 5.670 is the lattice constant of ZnSe (Å).[1] We fit the literature values (black dots) from reference 1 with equation (1) (red dashed curve), yielding a bowing parameter of 0.17 Å. This fit gives a direct correlation between the composition of the $ZnSe_zS_{1-z}$ shell and its lattice constant. We used the literature values[1] (black dots) to construct a continuous relationship between z and the lattice constant of $ZnSe_zS_{1-z}$ (red dashed curve) so that we can then extrapolate an *a* value for any given *z*.

ICP analysis on the In_xZn_yP/ $ZnSe_zS_{1-z}$ core/shell QDs confirmed that the actual composition of the shell (given by the Se% and S%), matches the ratios of the Se and S precursors used to grow the shell (defined by z). We measure these values for all the core/shell analysed in this manuscript. The results are summarized in table S3.

Table S4- Se% and S% ratio measured by ICP (OES) compared to the Se and S precursors used to grow the shell (defined by z).

Zn/In core	*z*	**Se (%)**	**S (%)**
1.8	1.0	1.00	0.00
1.8	0.8	0.81	0.19
1.8	0.6	0.63	0.37
1.8	0.2	0.29	0.71
1.8	0.0	0.00	1.00
2.0	1.0	1.00	0.00
2.0	0.8	0.85	0.15
2.0	0.4	0.65	0.35
2.0	0.0	0.00	1.00
2.7	0.6	0.69	0.31
2.7	0.4	0.54	0.46
2.7	0.5	0.57	0.43
2.7	0.0	0.00	1.00
2.4	1.0	0.00	1.00
2.4	0.6	0.67	0.33
2.4	0	0.00	1.00
3.7	0.8	0.86	0.14
3.7	0.24	0.39	0.61
3.7	0	0.00	1.00

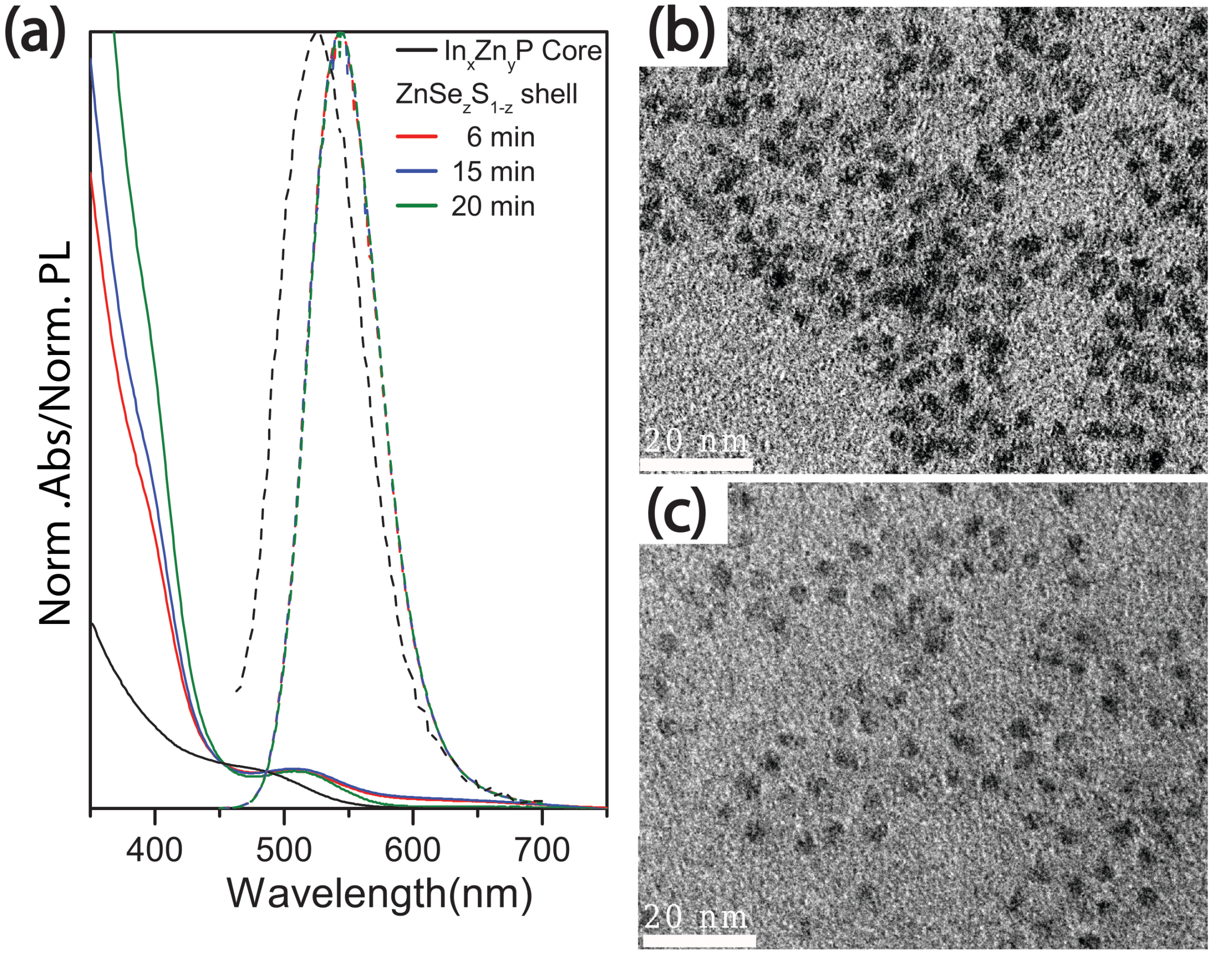

Figure S14- (a) Absorption (solid line) and PL spectra (dashed line) of In_xZn_yP and In_xZn_yP/ $ZnSe_zS_{1-z}$ core/shell NCs at different stages during the growth of the $ZnSe_zS_{1-z}$ shell, in the case of In_xZn_yP core with Zn/In:2.8 and *z*: 0.6. Upon shell growth a marked increase of the absorbance at wavelengths below 440 nm is observed. This wavelength corresponds to the band gap of bulk $ZnSe_zS_{1-z}$.[1] (b) TEM image of In_xZn_yP cores (up) and In_xZn_yP/ $ZnSe_zS_{1-z}$ core/shell QDs (down). The QDs have a size of d:2.8±0.2 nm and d:4.5±0.3 nm.

Table S5- Lattice constant of the core (a1) and shell (a2) (extrapolated by the curve in Figure S13 a), together with the respective QY of the core and core/shell QDs.

a_2 (Å)	a_1 (Å)	QY core (%)	QY C/S (%)
5.67	5.60	7	33.6
6.60	5.60	7	41.8
5.54	5.60	7	26.4
5.41	5.60	7	20.5
5.67	5.52	6.1	20.0
5.54	5.52	6.1	39.8
5.41	5.52	6.1	13.0
5.54	5.49	12	49.2
5.50	5.49	12	62.0
5.46	5.49	12	60.1
5.41	5.49	12	41.4
5.60	5.44	4.2	16.0
5.44	5.44	4.2	40.0
5.41	5.44	4.2	38.4
5.67	5.45	8.4	18.0
5.57	5.45	8.4	19.0
5.53	5.45	8.4	36.2
5.45	5.45	8.4	45.2
5.41	5.45	8.4	25.4

References

(1) Sadekar, H. K.; Ghule, A. V.; Sharma, R. Bandgap Engineering by Substitution of S by Se in Nanostructured ZnS1−xSex Thin Films Grown by Soft Chemical Route for Nontoxic Optoelectronic Device Applications. *J. Alloys Compd.* **2011**, *509*, 5525–5531.

(2) Denton, A.; Ashcroft, N. Vegard's Law. *Phys. Rev. A* **1991**, *43*, 3161–3164.

(3) Kats, A. Indium Phosphide Relat. Mater. Process. Technol. Devices, *Artech Hou.* **1992**

(4) Kuo, Y.-K.; Liou, B.-T.; Yen, S.-H.; Chu, H.-Y. Vegard's Law Deviation in Lattice Constant and Band Gap Bowing Parameter of Zincblende InxGa1−xN. *Opt. Commun.* **2004**, *237*, 363–369.